A two-parameter space to tune solid electrolytes for lithium dendrite constriction

Yichao Wang[1†], Luhan Ye[1†], Xi Chen and Xin Li[1*]

[1]John A. Paulson School of Engineering and Applied Sciences, Harvard University, Cambridge, MA 02138, USA

[†] Equal Contribution
[*] Corresponding author: lixin@seas.harvard.edu

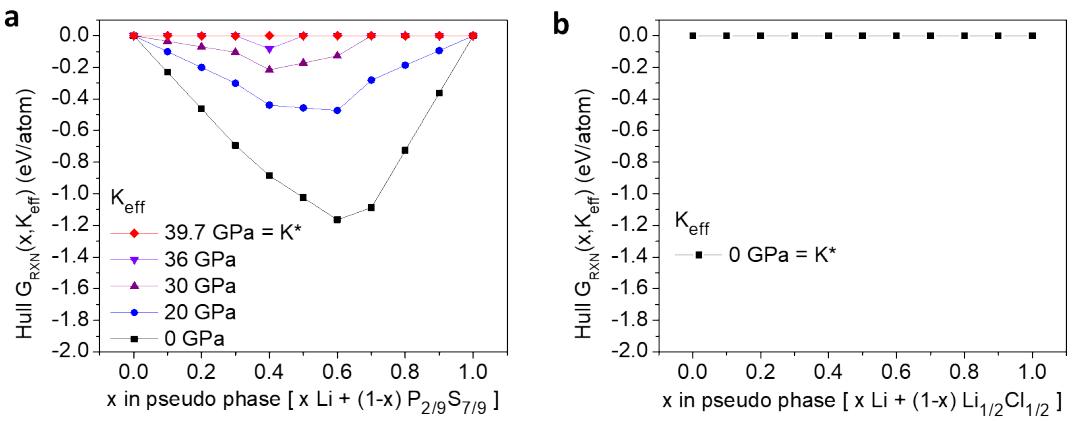

Fig. S1. Two examples to illustrate the calculation of K*. **a**, The unstable P_2S_7/Li interface; **b**, The stable LiCl/Li interface.

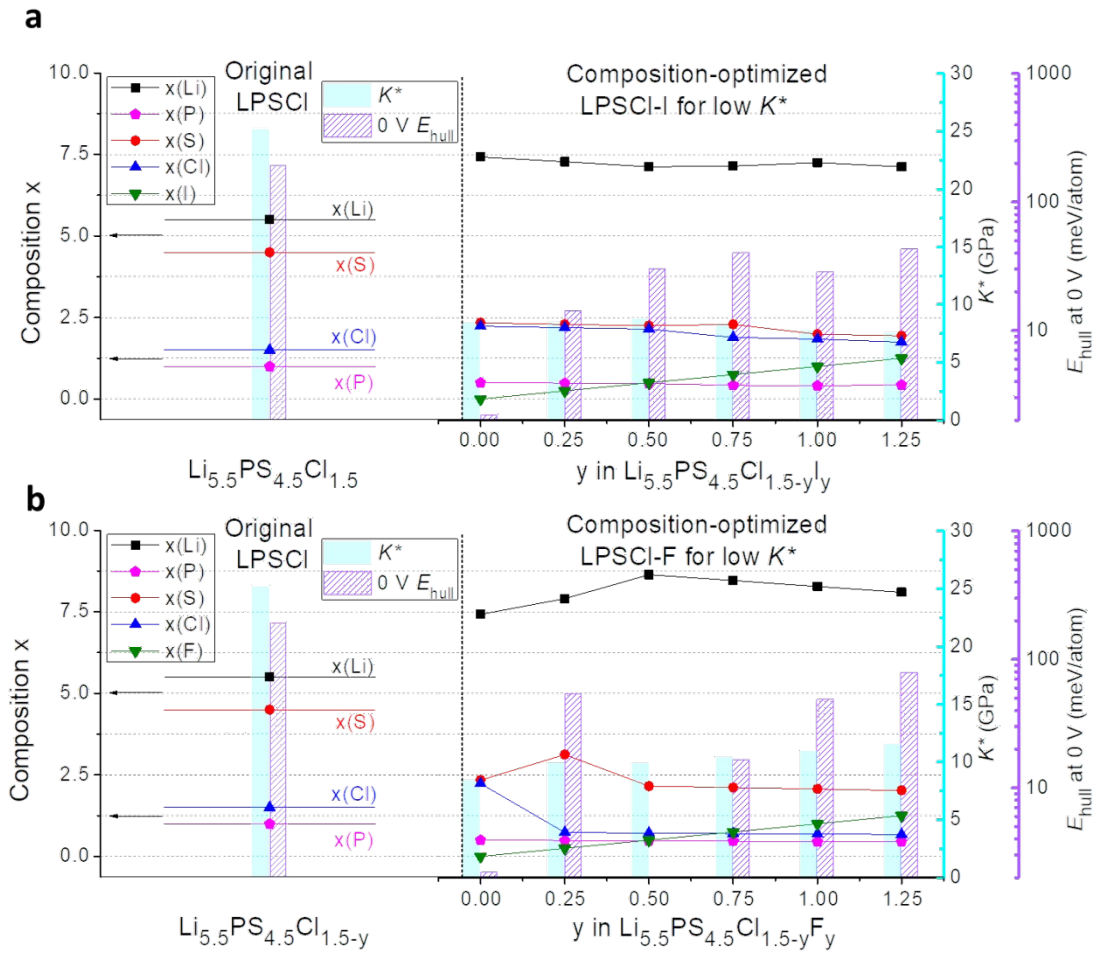

Fig. S2. Optimized composition, decomposition energy E_{hull} and critical modulus K^* at fixed dopant requirements for **a** LPSCl-I, and **b** LPSCl-F with minimized K^* (right panel). The left panel is for the values of original LPSCl without doping and minimization of K^*. LPSCl-I is optimized to be S, P deficient and Cl, Li rich. LPSCl-F is optimized to be S, P deficient and Li rich. At F deficient range, Cl can be either rich or deficient. Both K^* are low at around 10 GPa and decomposition energy can be increased up to a few tens of meV/atom.

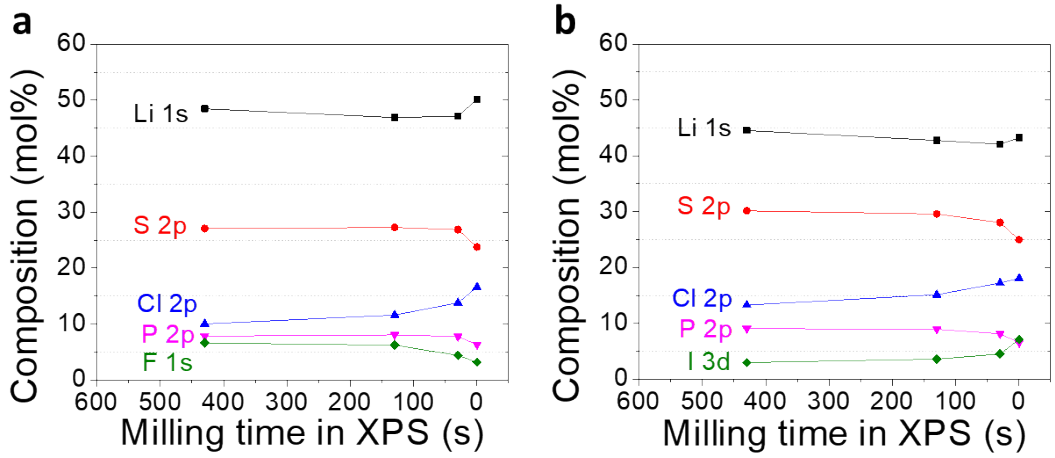

Fig. S3. XPS quantification of **a** LPSCl-F and **b** LPSCl-I.

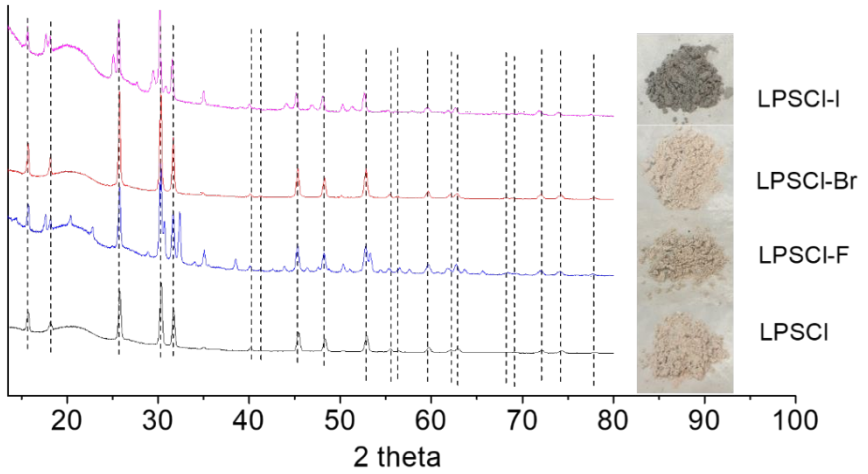

Fig. S4. XRD and optical photos of LPSCl and LPSCl-X (X = F, Br, I) powder. LPSCl and LPSCl-Br sample had a pure phase with F-43m space group, whose XRD reflections are marked by dashed line, while LPSCl-F and LPSCl-I have impurities.

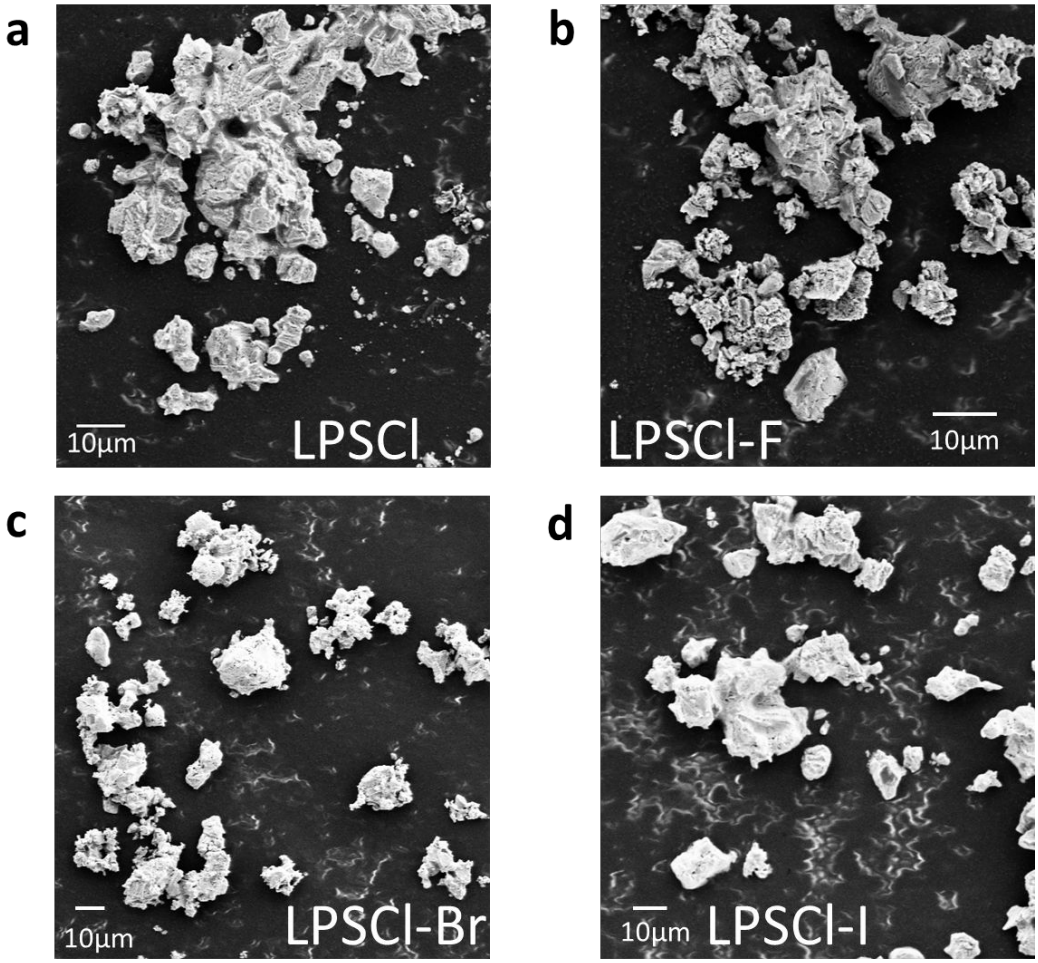

Fig. S5. SEM of **a** LPSCl, **b** LPSCl-F, **c** LPSCl-Br and **d** LPSCl-I. The particles have similar size of a few to ~30 µm.

Table S1. XPS of LPSCl and LPSCl-X with vacuum transfer sample holder. X-axis is energy (eV) and Y-axis is intensity.

	LPSCl	LPSCl-F	LPSCl-Br	LPSCl-I
Li	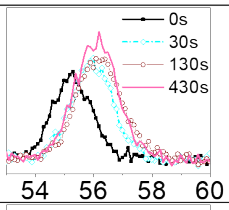	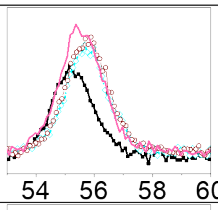	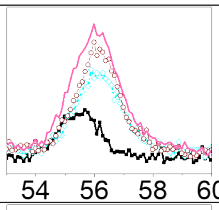	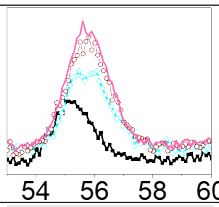
P	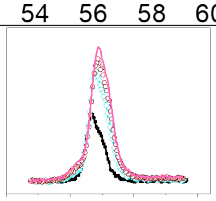	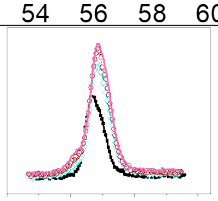	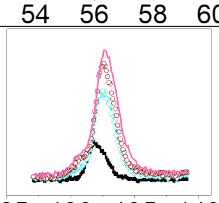	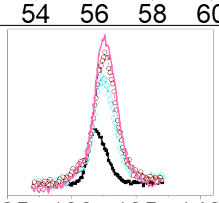
S	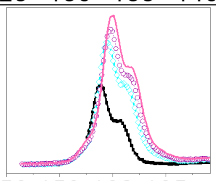	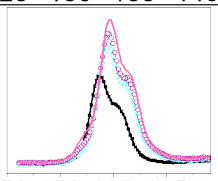	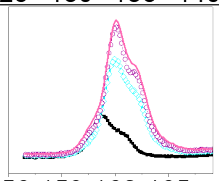	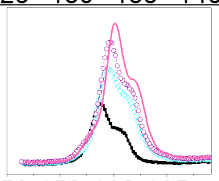
Cl	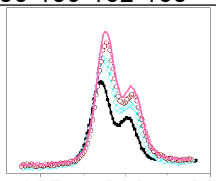	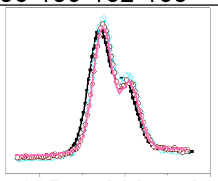	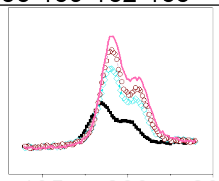	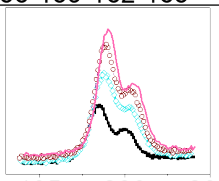
F Br I		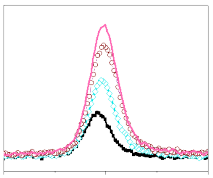	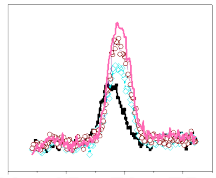	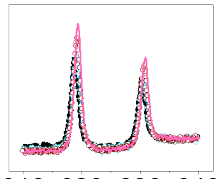

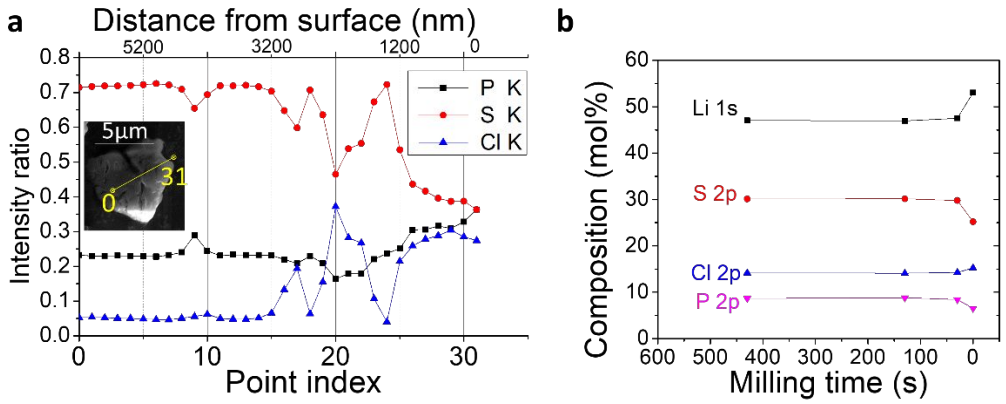

Fig. S6. Core shell structure of LPSCl characterized by SEM-FIB-EDS and XPS. **a**, Intensity ratio of Li, P, S and Cl and the inset shows the SEM image of the milled and line scanned particle. Index larger than 24 corresponds to points at the edge, where there is S deficiency and Cl richness. The same S deficiency and Cl richness observed in the point index range from 16 to 23 is also located at the edges of the particle cracks. **b**, XPS quantifications with milling show a S-deficient and Cl-rich shell.

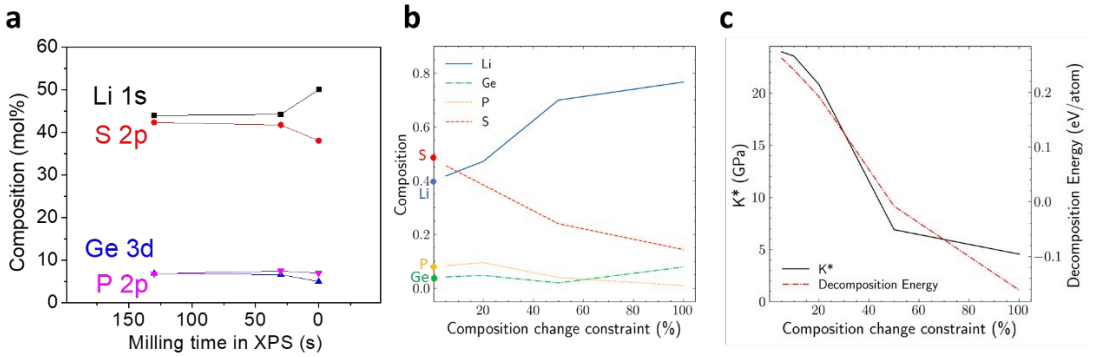

Fig. S7. a, XPS quantification at different depth of LGPS particles shows a Li rich, S, Ge, P deficient surface; **b**, machine learning optimized compositions with different allowed compositional change percentage for each element itself (composition change constraint), aiming for lower *K**. The zero point in x axis corresponds to the original LGPS. With larger allowed compositional changes, LGPS is optimized to be Li rich, S, Ge, P deficient, which is the same trend observed in the XPS quantification. **c**, Optimized *K** and the predicted decomposition energy with the same optimized composition. The 0.915 eV is the $Li_{0.49}Cl_{0.49}P_{0.01}S_{0.01}$ reference for zero DFT 0V decomposition energy. A relative small change in composition such as 30% can decrease the *K** to below 20 GPa along with a relatively large decomposition energy of 147 meV/atom.

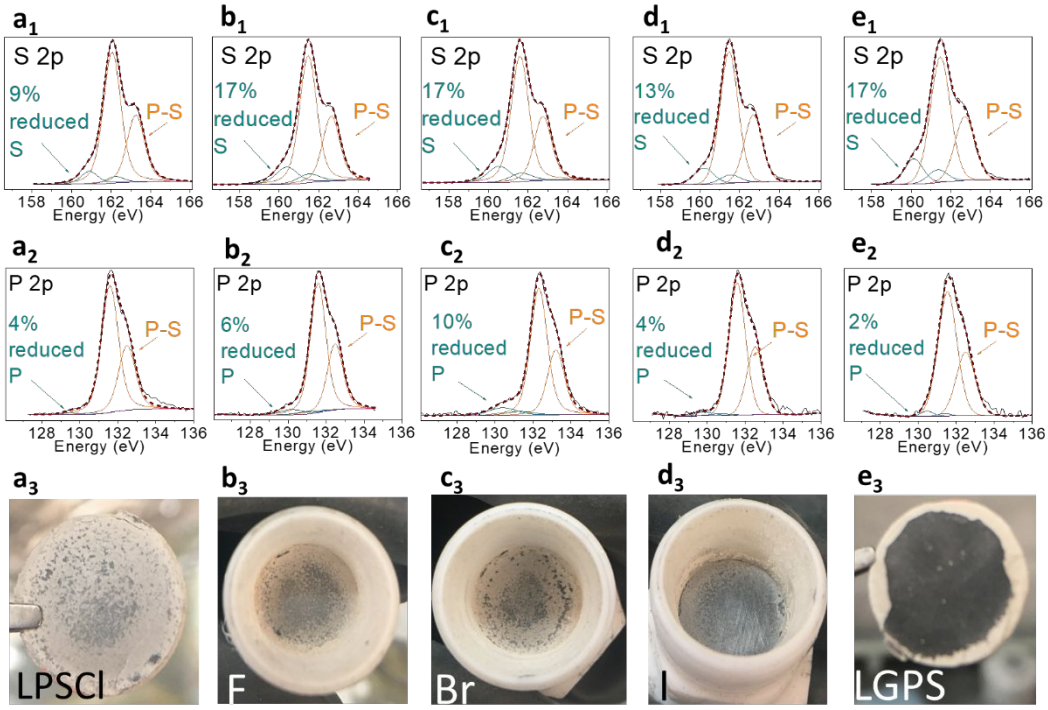

Fig. S8. XPS analysis and optical photos of the Li deposited **a**, LPSCl, **b**, LPSCl-F, **c**, LPSCl-Br, **d**, LPSCl-I and **e**, LGPS. XPS analysis shows that the decomposition is the weakest for the Li deposited LPSCl with least S reduction and limited P reduction, while the reduction of S becomes stronger for LPSCl-X and LGPS, and LPSCl-F and LPSCl-Br have stronger P reduction. Therefore, the gray and silver color of $\mathbf{a_3}$ Li deposited LPSCl should be largely from Li metal, while the larger area of dark gray color of $\mathbf{b_3}$ to $\mathbf{d_3}$ Li deposited LPSCl-X and the black color of $\mathbf{e_3}$ Li-deposited LGPS should be from decompositions.

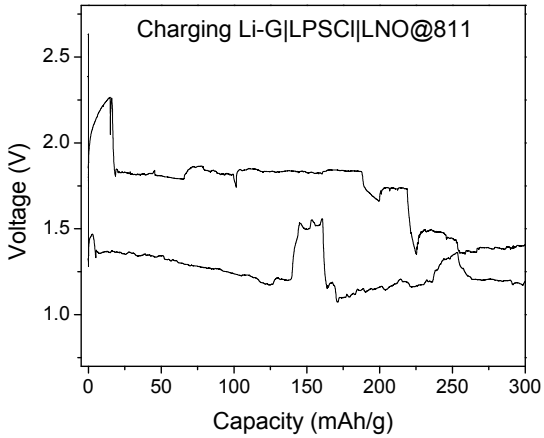

Fig. S9 Two other Li-G|LPSCl|LNO@811 batteries that failed during intial charging with sudden voltage drop followed by noisy voltage curve, indicating shorting cuased by Li dendrite pennetration.

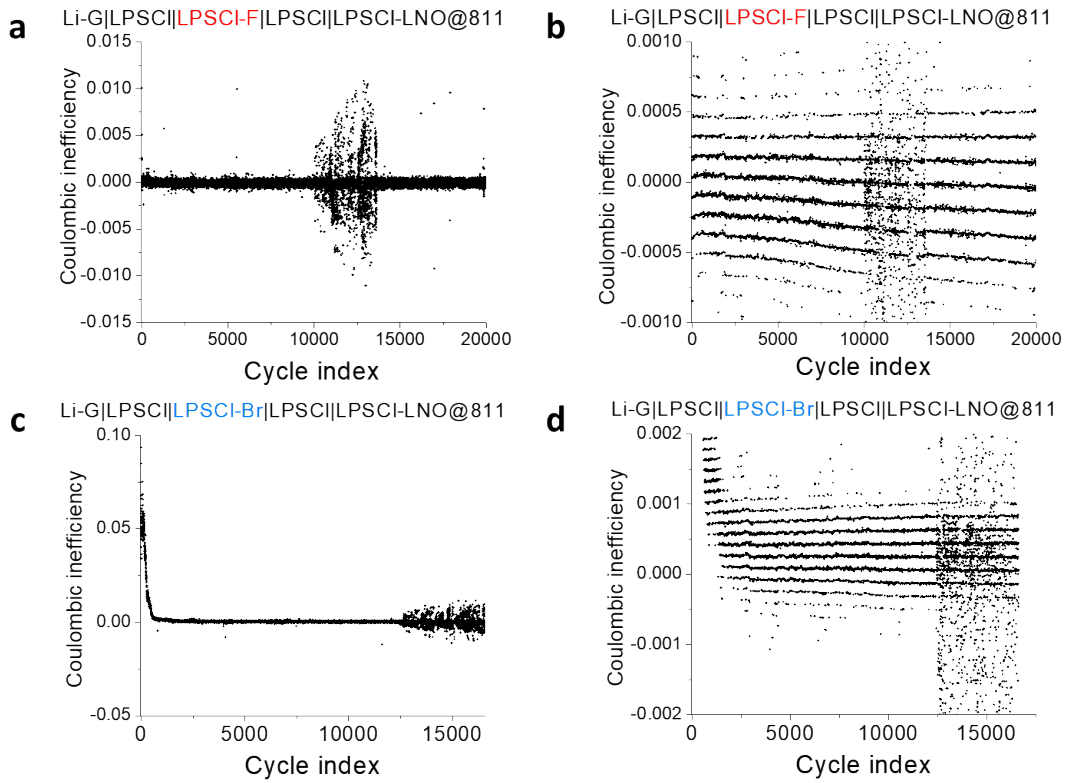

Fig. S10. 20 C-rate cycling Coulombic inefficiency of **(a** and **b)** Li-G|LPSCl|LPSCl-F|LPSCl|LNO@811 at large scale (**a**) and small scale (**b**), and of **(c** and **d)** Li-G|LPSCl|LPSCl-Br|LPSCl|LNO@811 at large scale (**c**) and small scale (**d**).

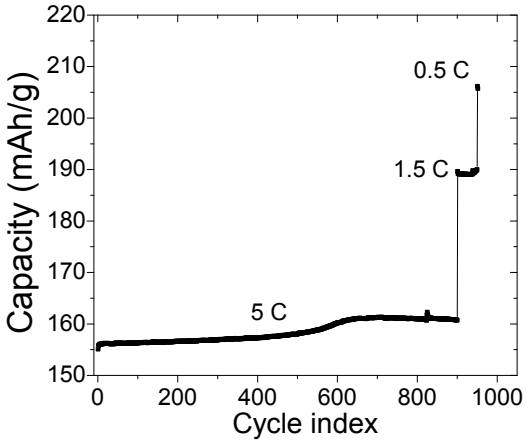

Fig. S11. Cycling performance at different low rates of Li-G|LPSCl|LPSCl-I|LGPS|811.

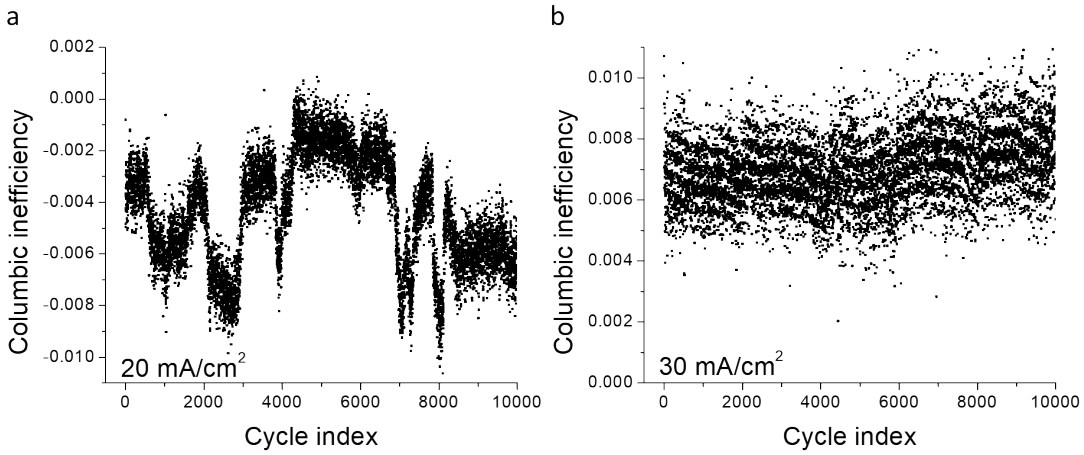

Fig. S12 Coulombic inefficiency of Li-G|LPSCl|LPSCl-I|LGPS|811 at **a**, 20 mA/cm^2, and **b**, 30 mA/cm^2.

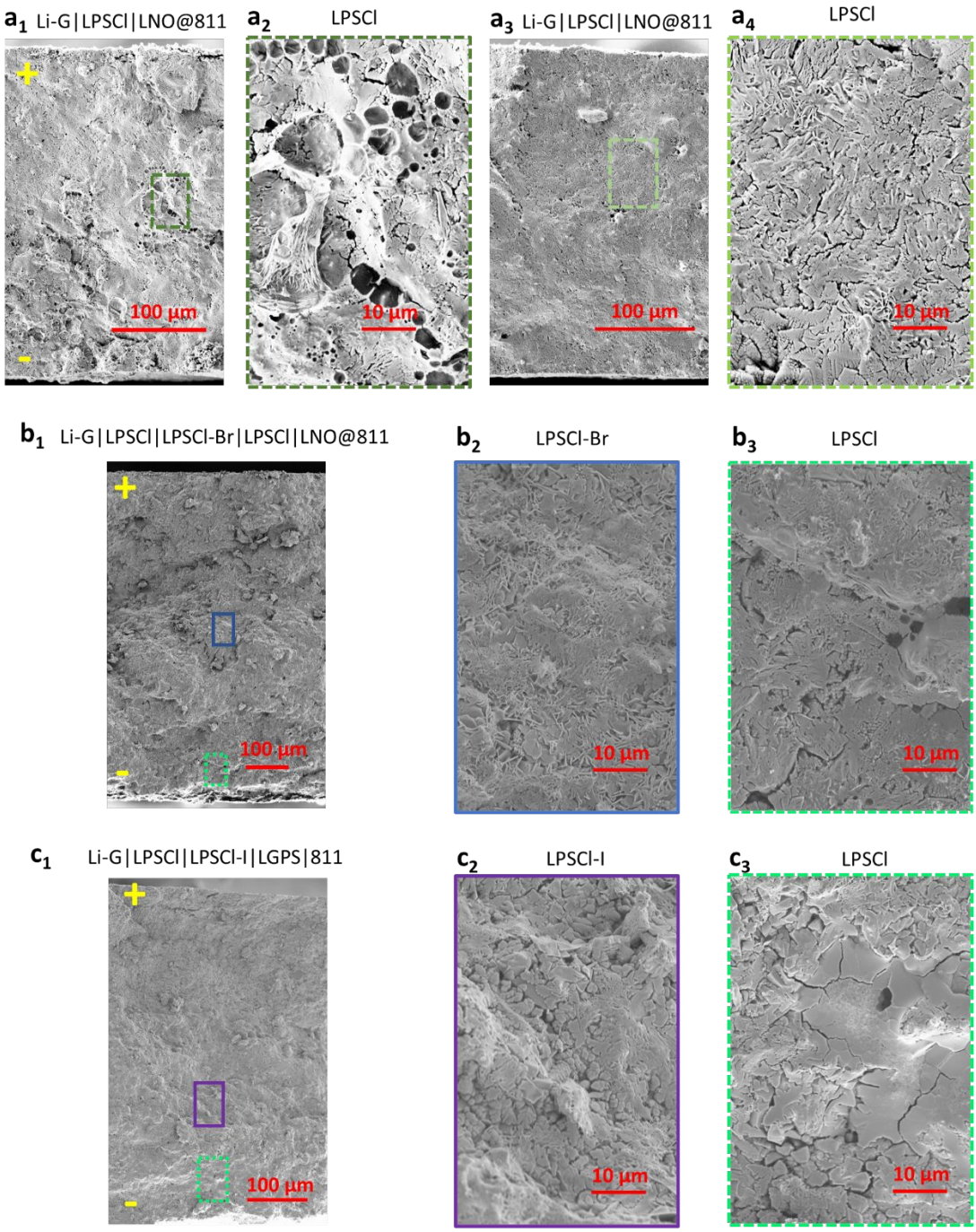

Fig. S13 SEM image of cycled battery pellet cross section. The cathodes are on the top and the anodes are on the bottom. (a1-a4) The cross sections of 8.6 mA/cm^2 cycled Li-G|LPSCl|LNO@811 battery (green data in Figure 4B and D) and magnified views of LPSCl layer showing that there are macro pores and microcracks network in the LPSCl layer after cycling; (b1) The cross section of 8.6 mA/cm^2 cycled Li-G|LPSCl|LPSCl-Br|LPSCl|LNO@811 battery (Figure 4C and blue data in 4D), and magnified views of (b2) LPSCl-Br layer and (b3) anode side LPSCl layer, showing that LPSCl-Br layer is compact without large pores and cracks, while the LPSCl layer morphology is more similar to that in (a); (c1) The cross section of 30 mA/cm^2 cycled Li-G|LPSCl|LPSCl-Br|LPSCl|LNO@811 battery (darker blue in Figure 5D), and magnified views of (c2) LPSCl-I layer and (c3) anode side LPSCl layer. Though there are

few small isolated microcracks in the LPSCl-I layer, there is no macro pores and microcracks network as observed in LPSCl in (a). The anode side LPSCl layer is more similar to that in (a).

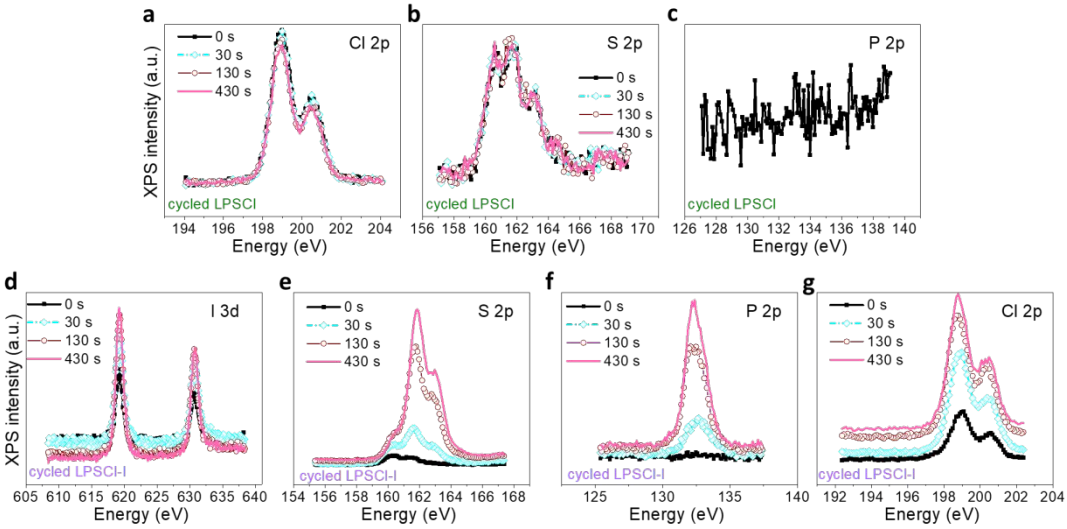

Fig. S14 XPS of the cross section of cycled battery pellet with ion-milling. (a-c) Cl 2p, S 2p and P 2p XPS evolution during ion-milling for cycled LPSCl; Cl 2p and S 2p peaks barely change over the milling duration, which are consistent with the unchanged composition during milling in Figure 6, and P 2p has almost no intensity due to low composition. (d-g) I 3d, S 2p, P 2p and Cl 2p XPS evolution during ion-milling for cycled LPSCl-I. The intensity increase is consistent with the composition change in Figure 6.

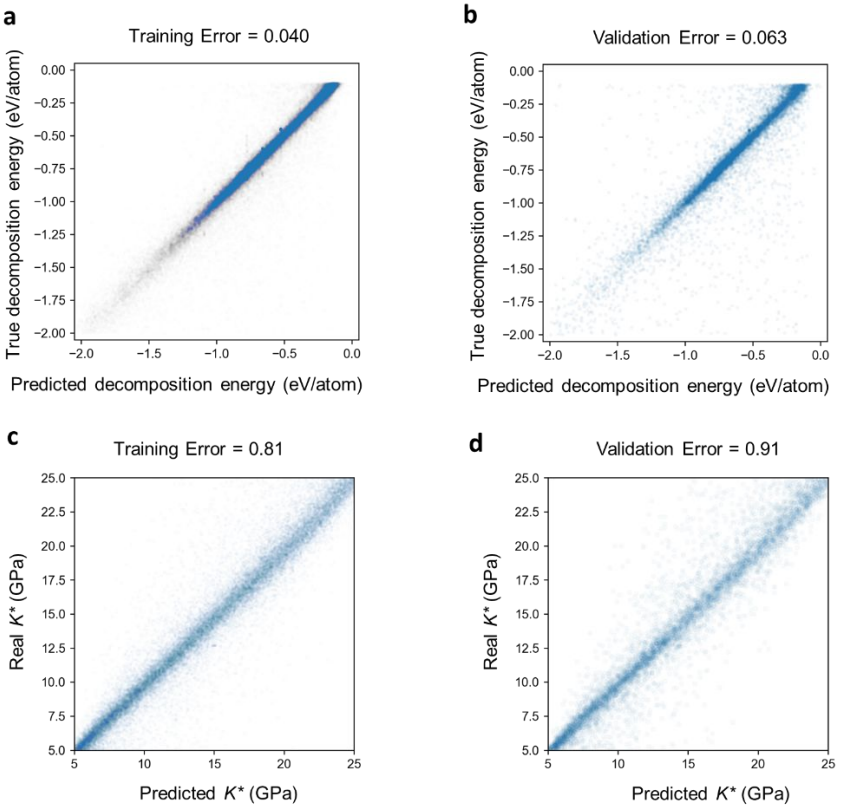

Fig. S15 Training and validation error for modelling (a,b) decomposition energy and (c,d) K^*.

The difference between the training error and validation error describes the error associated with generalization to unseen data.

More Details about Machine Learning

Compositions, energies and volumes of all 124,497 materials are queried from Materials Project for high throughput calculations of decomposition energies (E_{hull}) and critical modulus (K^*) values for the interfaces between materials and Li metal. Machine learning is applied to model the relation between macroscopic properties (composition, energy, volume) and target values (E_{hull}, K^*). Machine learning models in this work are based on decision trees. A decision tree consists of hierarchical computation (decision) nodes. The input data to the decision trees is in the form $(X,y) = (\{x_1,x_2,...,x_n\},y)$ where x_i are the features and y is a target value. The decision tree can perform both the regression and classification tasks, depending on whether the nature of target variable y being continuous or a finite number of classes. Starting with the input features, each node of the tree applies a conditional statement on the value of a feature, then moves to a subsequent node based on the truth of that statement. The optimization of the tree includes choosing both the feature and threshold for the criteria for each node that overall best splits the set of items. Instead of measuring the error, better metrics such as the cross entropy and the Gini index are generally used to measure the goodness of the choice of criteria and data split.[1] Our input features X consist of the 103-dimensional composition vectors of the first 103 elements in the Periodic Table up to lawrencium (Lr). The composition vector is normalized with the sum equals to one. Specifically, for K^* at 0 V, we also include the x from 0 to 0.9 in our input for a better learning result. The target y are chosen as the K^*, and decomposition energy at different situations. For K^* at 0 V, the target y is the K^* at the corresponding x. We use an ensemble model of individual decision trees, the Extremely Randomized Tree model. In such models, a number of N trees are initialized simultaneously ($N = 30$ in our setting). Each tree in the ensemble is fed with training data sampled from the training set. A random subset of candidate features is used, from which thresholds are drawn at random for each candidate feature, and the best of these randomly generated thresholds is picked as the splitting rule.

We split the data into 80:20 training and validation sets. For both K^* and E_{hull}, our models achieve low training error and comparable validation error (Figure S15). The composition – target quantity relation is fitted well, with little overfitting. Using the trained models with target property y, we can predict y at unknown compositions. We obtain the composition with optimal y using the grid search. Optimization with fixed F/Br/I in Figure 1C and Figure S2 are with 50% relative compositional change constraint on each element to avoid extinction of certain elements. Since most compounds are unstable with Li metal so that the zero hull energy data are insufficient in the training set, the machine learning predicted zero hull energy reference has to be calibrated by DFT. LiCl shows a ~ 0 eV decomposition energy with Li metal in DFT binary calculations (Figure S1), and the predicted decomposition energy for $Li_{0.49}Cl_{0.49}S_{0.01}P_{0.01}$ is 0.915 eV, so the decomposition energy is shifted down by 0.915 eV in Figure 1C, Figure S2 and Figure S7.

Reference

1. Bishop, C. M., *Pattern recognition and machine learning*. springer: 2006.